






The Mission Accessible Near-Earth Objects Survey: Four Years of Photometry

Audrey Thirouin¹ , Nicholas A. Moskovitz¹ , Richard P. Binzel², Eric J. Christensen³, Francesca E. DeMeo², Michael J. Person², David Polishook⁴, Cristina A. Thomas^{5,6}, David Trilling⁶ , Mark C. Willman⁷, Brian Burt¹, Mary L. Hinkle^{6,8}, and Teznie Pugh¹

¹Lowell Observatory, 1400 West Mars Hill Road, Flagstaff, Arizona 86001, USA; thirouin@lowell.edu

²Massachusetts Institute of Technology (MIT), 77 Massachusetts Avenue, Cambridge, Massachusetts 02139, USA

³Lunar and Planetary Laboratory, Department of Planetary Sciences, University of Arizona, Tucson, Arizona 85721, USA

⁴Department of Earth and Planetary Science, Weizmann Institute, Herzl St 234, Rehovot, 7610001, Israel

⁵Planetary Science Institute (PSI), 1700 East Fort Lowell Road 106, Tucson, Arizona 85719, USA

⁶Northern Arizona University (NAU), San Francisco Street, Flagstaff, Arizona 86001, USA

⁷University of Hawaii, Pukalani, Hawaii 96788, USA

⁸University of Central Florida (UCF), 4000 Central Florida Boulevard, Orlando, Florida 32816, USA

Received 2018 July 27; revised 2018 September 6; accepted 2018 September 10; published 2018 November 5

Abstract

Over 4.5 years, the Mission Accessible Near-Earth Object Survey assembled 228 near-Earth object (NEO) light curves. We report rotational light curves for 82 NEOs, constraints on amplitudes and periods for 21 NEOs, light curves with no detected variability within the image signal-to-noise and length of our observing block for 30 NEOs, and 10 tumblers. We uncovered two ultra-rapid rotators with periods below 20 s,—2016 MA with a potential rotational periodicity of 18.4 s, and 2017 QG₁₈ rotating in 11.9 s—and estimated the fraction of fast/ultra-rapid rotators undetected in our project plus the percentage of NEOs with a moderate/long periodicity undetectable during our typical observing blocks. We summarize the findings of a simple model of synthetic NEOs to infer the object’s morphology distribution using the measured distribution of light curve amplitudes. This model suggests that a uniform distribution of axis ratio can reproduce the observed sample. This suggests that the quantity of spherical NEOs (e.g., Bennu) is almost equivalent to the quantity of highly elongated objects (e.g., Itokawa), a result that can be directly tested thanks to shape models from Doppler delay radar imaging analysis. Finally, we fully characterized two NEOs—2013 YS₂ and 2014 FA₇—as appropriate targets for a potential robotic/human mission due to their moderate spin periods and low Δv .

Key words: minor planets, asteroids: general

Supporting material: figure sets, machine-readable table

1. Mission Accessible Near-Earth Object Survey (MANOS): Presentation

Our MANOS project started about 4.5 years ago and aspires to characterize mission accessible near-Earth objects (NEOs). Our project is designed to fully characterize NEOs, providing rotational light curves, visible and/or near-infrared reflectance spectra and astrometry. Such an exhaustive study will give us the opportunity to derive general properties regarding compositions, and rotational characteristics. Because existing physical characterization surveys have primarily centered on the largest NEOs with sizes above 1 km, MANOS mainly targets sub-km NEOs (Benner et al. 2015; Li et al. 2015; Reddy et al. 2015; Thirouin et al. 2016).

Our project is split into two main parts: (i) *spectroscopy* to provide surface composition, spectral type, taxonomic albedo and infer the object’s size; and (ii) *photometry* to provide rotational properties and astrometry. Below, we center our attention on the rotational characteristics of the MANOS NEOs extracted from the photometry.

Here, we present new data combined with results from Thirouin et al. (2016). Thanks to this homogeneous sample of 228 NEOs, we can perform statistical studies and understand the rotational characteristics of the small NEOs in comparison to the larger NEOs. In Sections 2-4, we briefly present our survey strategy and data analysis, in addition to presenting our light curves. Sections 5 and 6 respectively feature our results derived from the light curves and their implications. Section 7 details our simple model for creating three synthetic

populations of light curves assuming different axis ratio distributions for comparison with the literature and our observations. The last section summarizes our conclusions.

2. MANOS: Observing Plan, Facilities, Data Analysis

In approximately 4.5 years, MANOS observed 308 NEOs for light curves (86 objects in Thirouin et al. 2016; 142 here, and the remainder will be reported in a future work). Figure 1 summarizes the objects observed by MANOS with NEOs from the LCDB⁹ (Warner et al. 2009). The LCDB contains 1359 entries for NEOs, and 1147 have a rotation estimate (objects with a constraint for the period are not considered). The LCDB distribution peaks at $H \sim 17$ mag (i.e., NEO with a diameter of $D \sim 1$ km for a geometric albedo of 20%, Pravec & Harris 2007), whereas for the MANOS sample the peak is at $H \sim 24$ mag (i.e., $D \sim 45$ m).

MANOS employs a set of 1–4 m telescopes for photometric purposes: the 1.3 m Small and Moderate Aperture Research Telescope System (SMARTS) telescope at CTIO, the 2.1 m and the 4 m Mayall telescopes at Kitt Peak Observatory, the 4.1 m Southern Astrophysical Research (SOAR) telescope, and the Lowell’s Observatory 4.3 m Discovery Channel Telescope (DCT). A complete description of these facilities, the instruments used, and filters, is available in Thirouin et al. (2016). In 2016 January, Mosaic-1.1 was replaced by Mosaic-3 at the Mayall telescope. This new instrument is also a wide-field

⁹ Light-curve database (LCDB) from 2017 November.

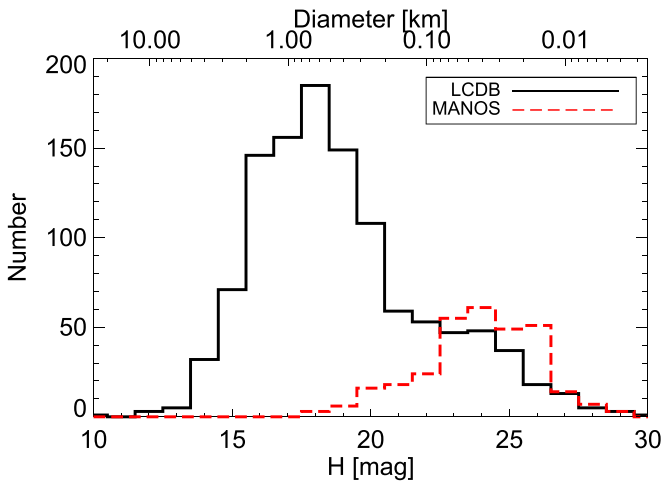


Figure 1. The continuous black line summarizes the NEOs from the literature compiled by Warner et al. (2009), whereas our red discontinuous line represents our MANOS sample observed over the past ~ 4.5 years. We use a “by-default albedo” of 20% to estimate the diameter (Warner et al. 2009).

imager with four 4096×4096 CCDs for a $36' \times 36'$ field of view and $0''.26/\text{pixel}$ as scale.

Our observing method and data reduction/analysis are summarized in Thirouin et al. (2016). Periodograms are in Figure 6.1 in Appendix A and light curves¹⁰ are in Figure 6.7 and 7.1 and in Appendix B. Typical photometric error bars are ± 0.02 – 0.05 mag, but can be larger in some cases, especially with small facilities, faint objects, or fast-moving objects.

3. MANOS: Photometry Summary

For this work, we classified the light curves in four main categories: (i) *full light curve* with a minimum of one entire rotation or a large portion of the light curve to estimate a periodicity, (ii) *partial light curve* showing a decrease or increase of the visual magnitude, but with not enough data for a period estimate, (iii) *flat light curve* with no obvious increase/decrease in variability and no period detected, and (iv) *potential tumbler* with or without the primary period (or shortest period, Pravec et al. 2005). We have full light curves for 82 NEOs¹¹ ($\sim 57\%$ of our data set), lower limits for periodicity and amplitude for 21 NEOs ($\sim 15\%$), flat light curves for 30 NEOs ($\sim 21\%$), and 10 NEOs are potential tumbler ($\sim 7\%$) (see Figure 2). We present two light curves (one flat and one full) for 2014 WU₂₀₀. This case will be discussed below.

MANOS found the fastest known rotator so far, 2017 QG₁₈ with a rotation of 11.9 s. This object was imaged at DCT in 2017 August, and the light curve has a variability of about 0.21 mag. The typical photometry error bar is 0.05 mag. We discovered the potential ultra-rapid rotator: 2016 MA. MANOS observed this object in 2016 June, and measured a short period of 18.4 s. The typical photometry error bar is 0.05 mag. The light curve displays low variability with a full amplitude of 0.12 mag. Unfortunately, the confidence level of this periodicity is low (i.e., $< 99.9\%$ confidence level stated for a period estimate) and more data are required to infer if 2016 MA is a

¹⁰ Light curves and photometry files can be found at manos.lowell.edu.

¹¹ We have 2 light curves for 2014 WU₂₀₀. Only the full light curve is considered for these estimates.

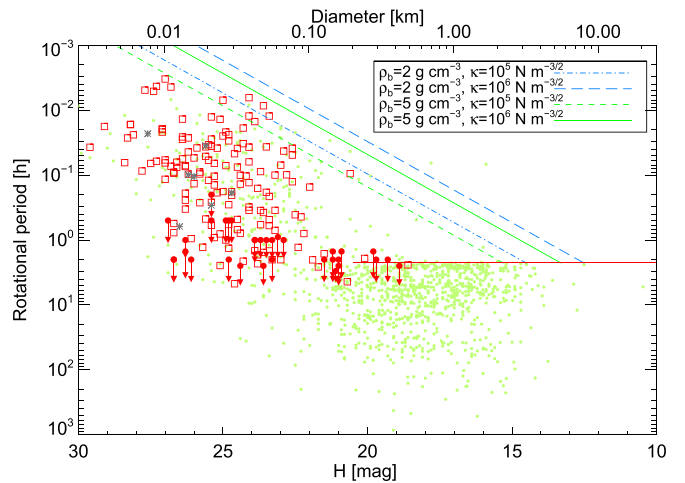


Figure 2. MANOS objects with a full light curve (red squares), NEOs with a lower limit to their rotations (red arrows), and tumbler (gray asterisks) are plotted. The red continuous line is the spin barrier at ~ 2.2 hr. The blue and green lines are the maximum spin limits, assuming different densities and tensile strength coefficients. NEOs from the LCDB are also plotted (green circles).

ultra-rapid rotator or not. In summary, MANOS discovered four ultra-rapid rotators with periodicities below 20 s: 2014 RC, 2015 SV₆, 2016 MA, and 2017 QG₁₈ (Thirouin et al. 2016, and this work).

3.1. Asymmetric/Symmetric and Complex Light Curves

Only three NEOs display a symmetric light curve, 2014 UD₅₇, 2014 WF₂₀₁, and 2017 LD, whereas 66 have a bimodal light curve with two different peaks¹² (i.e., asymmetric curve). The majority of the MANOS NEOs have an asymmetry < 0.2 mag, but sometimes, the difference is higher: 2013 SR and 2015 KQ₁₂₀ with an asymmetry of ~ 0.5 mag, 2014 FF with ~ 0.3 mag, 2014 HN₁₇₈ with ~ 0.4 mag, and 2014 KH₃₉ with ~ 0.7 mag.

Thirteen objects have complex light curves that cannot be fit with only two harmonics: 2014 HS₁₈₄, 2014 HW, 2016 BF₁, 2016 DK, 2016 ES₁, 2017 EK, 2017 EZ₂, 2017 HV₃, 2017 JM₂, 2017 KZ₂₇, 2017 LE, 2017 MO₈, and 2017 QX₁. The reasons for this morphology are as follows: (i) complex shape (NEOs far from spherical/ellipsoidal shapes), and/or (ii) albedo contrast, and/or (iii) satellite. More observations in different geometries will be useful for shape modeling and to probe for a companion. Unfortunately, most of them will not be brighter than 21 mag in the upcoming decade.

3.2. Partial Light Curves

Twenty-one objects display an increase/decrease in magnitude (red arrows Figure 2). We did not calculate a secure periodicity because our observations spanned less than 50% of the NEO’s rotation. For example, 2016 JD₁₈ was imaged with Lowell’s DCT for a span of ~ 0.5 hr. The partial light curve presents a large amplitude of ~ 1.2 mag and a feature possibly suggesting a complex shape.

¹² Tumblers are not considered in this subsection.

3.3. Tumblers

We found ten potential tumblers: 2013 YG, 2014 DJ₈₀, 2015 CG, 2015 HB₁₇₇, 2015 LJ, 2016 FA, 2016 RD₃₄, 2017 EE₃, 2017 HU₄₉, and 2017 QW₁. We derive their main periodicities and report them in Table 1. For three of them, we are not capable of deducing the main period. In all cases, our data were insufficient to derive the second period with the Pravec et al. (2005) technique.

3.4. Flat Light Curves

Thirty objects have no detected periodicity in the measured photometry. These flat light curves can be due to: (i) a long/very long periodicity that was not detected over our observing window, (ii) a rapid rotation consistent with the exposing time, (iii) a (nearly) pole-on configuration, or (iv) a NEO with a spheroidal shape. Below, we discuss these four scenarios by assuming that all small NEOs are fast rotators and large NEOs are slow rotators. Such an assumption is based on the well-known rotational period-size relation (Figure 2), but it is important to emphasize that our assumption may not be right for all objects, as some small objects have been found to be slow rotators (Warner et al. 2009). Thus, MANOS can be identifying slow or fast rotators in the small size range.

4. Flat Light Curves: Four Scenarios

4.1. Slow Rotators

As we only dedicate a short observing block per object (typically $\sim 2\text{--}3$ hr, or shorter in case of weather or technical issues), we are biased against long rotational periods (typically, longer than 5–6 hr). Five objects from this work and Thirouin et al. (2016) were observed by other teams that derived the following rotation periods: 1994 CJ₁ (~ 30 hr, Warner 2015b), 2008 TZ₃ (44.2 hr, Warner et al. 2009), 2013 YZ₃₇ (8.87 hr, Warner 2014), 2014 SM₁₄₃ (2.9 hr, Warner 2015c), and 2015 LK₂₄ (18.55 hr, Warner 2015a). For 2014 SM₁₄₃, the Warner (2015c) observations and ours are separated by about 8–10 days. In both cases, data were obtained at high phase angle ($> 50^\circ$). We observed 2014 SM₁₄₃ over ~ 2.5 hr with a typical photometric error bar of 0.1 mag and should have detected such a period, assuming that the period derived by Warner (2015c) is correct. However, Warner (2015c) presented a noisy photometry and their period spectrum showed several solutions that were marginally significant. Therefore, the authors are not confident about their results, and the reported period could be wrong. Our results for 2014 SM₁₄₃ are available in Thirouin et al. (2016).

We expect “large” objects with $D > 100$ m (i.e., $H > 22.4$ mag) to have a slow rotation (Figure 2). Therefore, 2004 BZ₇₄, 2005 RO₃₃, 2007 CN₂₆, 2008 HB₃₈, 2010 CF₁₉, 2011 ST₃₂₃, 2011 WU₉₅, 2012 ER₁₄, 2012 XQ₉₃, 2014 CP₁₃, 2014 OA₂, and 2014 YD₄₂ are probably slow rotators with periods undetected over our short sampling. 2013 UE₃, and 2016 AU₆₅ ($H = 22.7$ mag, and 22.9 mag, respectively) are likely slow rotators too (Figure 2). There are no other published data on these objects for comparison to our results. The length of our observing blocks is the lower limit for their periods.

In conclusion, 19 large objects ($D \gtrsim 100$ m) in the full MANOS sample are potential slow rotators (i.e., $\sim 8\%$ of the full sample reported in Thirouin et al. (2016) and here). Thus, we estimate that at least 43% of our flat light curves from this

work and our previous paper are caused by slow rotation undetectable over our typical observing blocks. It is crucial to mention that for this estimate, we consider that all large objects are slow rotators, which may not be the case for all of them.

4.2. Pole-on Orientation

Pole orientations are known for a handful of large NEOs with diameters of several km (e.g., La Spina et al. 2004; Benner et al. 2015; Vokrouhlický et al. 2015). Shape modeling with radar observations and/or light curves obtained at different epochs are required to estimate the pole orientation. MANOS targets typically fade in a matter of hours or days, and their next optical window is often decades away, so light curves at different epochs/observing geometries are generally not feasible. For fast and small rotators, radar techniques cannot construct the object’s shape, and thus no pole orientation is derived.

The pole orientation distribution of large objects in the main belt of asteroids (MBAs) is isotropic, whereas small MBAs and NEOs ($D < 30$ km) have preferentially retrograde/prograde rotation (La Spina et al. 2004; Hanuš et al. 2013; Vokrouhlický et al. 2015). Vokrouhlický et al. (2015) reported 38 pole solutions with an excess of retrograde-rotating NEOs, and noticed a clear deficit of small MBAs and NEOs with a pole orientation of 0° . The MANOS set is mostly composed of NEOs in the sub-100 m range, and unfortunately, there is no comprehensive information about pole orientation for this size range. However, if the sub-100 m NEOs follow the same trend as small main-belt asteroids and large NEOs, then we expect an excess of small bodies with a pole orientation of $\sim \pm 90^\circ$.

If the rotation axis of an elongated NEO and the sight line are (nearly) aligned, the brightness variation due to its rotation will be undetectable. Depending on the aspect angle (θ), the light-curve amplitude of an elongated object ($a > b > c$) is:

$$\Delta m = 2.5 \log \sqrt{\frac{\bar{a}^2 \cos^2 \theta + \bar{a}^2 \bar{c}^2 \sin^2 \theta}{\bar{a}^2 \cos^2 \theta + \bar{c}^2 \sin^2 \theta}}, \quad (1)$$

where $\bar{a} = a/b$, $\bar{b} = 1$, and $\bar{c} = c/b$. The likelihood of observing an object pole-on is $P = 1 - \cos \theta$ (Lacerda & Luu 2003). As an example, the probability of viewing a small body with a pole-on orientation $\pm 5^\circ$ is $< 1\%$. Therefore, we estimate that only a few if any of our flat light curves are due to a pole-on orientation.

4.3. Spherical Objects

Using the previous equation, the largest amplitude will be at $\theta = 90^\circ$, and the smallest will be at $\theta = 0^\circ$ and 180° . At $\theta = 90^\circ$, $\Delta m = 2.5 \log(\bar{a})$. Therefore, the brightness variability of an almost spherical object will be flat. As noted, shape modeling using radar observations and/or light curves at different epochs are required to derive the object’s shape. However, there are very few shape models available for sub-100 m NEO (Benner et al. 2015).

Several NEOs with $D > 200$ m have an oblate shape with a ridge at the equator or a diamond shape, and they are predicted to be relatively common (Benner et al. 2015). Objects like Bennu, 2008 EV₅, 2004 DC, 1999 KW₄, and 1994 CC have an oblate shape based on radar observations, and a low to moderate light curve amplitude with periods longer than 2 hr (Ostro et al. 2006; Pravec et al. 2006; Taylor 2009; Warner et al. 2009; Brozović et al. 2011; Busch et al. 2011; Nolan et al. 2013;

Table 1
Observing Log and Results^a

NEO	UT-Date	Nb _{im}	r_h (au)	Δ (au)	α (°)	Filter	Tel	ΔT (minutes)	t_{exp} (s)	Rot. P. (hr)	Δm (mag)	φ_0 (2450000+)	H	D (m)	Dyn. class	Δ_V^{SH} (km s ⁻¹)	Δ_V^{NHATS} (km s ⁻¹)
<i>Full light curve</i>																	
<i>Symmetric</i>																	
2014 UD ₅₇	2014 Oct 28	182	1.022	0.028-0.029	9.8-9.6	wh	KP4	153	20	0.0959	0.88 ± 0.02	6958.62714	25.8	20	Apollo	5.19	11.278
2014 WF ₂₀₁ ^b	2014 Dec 01	44	1.010	0.028	29.4-29.5	wh	KP4	28	10	0.4743	0.46 ± 0.05	6992.62728	25.6	22	Apollo	5.10	7.094
2017 LD	2017 Jun 04	53	1.022	0.0082	15.9-16.1	VR	DCT	21	3	0.0660	0.47 ± 0.04	7908.83057	27.5	9	Amor	4.47	8.339
<i>Asymmetric</i>																	
1999 SH ₁₀	2014 Mar 28	178	1.120	0.147-0.146	31.7	wh	KP4	201	35	0.1264	0.29 ± 0.03	6744.87878	22.6	89	Apollo	5.57	8.634
2006 HX ₃₀	2015 May 27	73	1.049-1.050	0.040	24.7	r'	SOAR	93	20	0.0966	0.41 ± 0.03	7169.74255	26.2	17	Amor	4.72	10.456
2010 MR	2014 Jul, 11–14, 14–21	126	1.494-1.432	0.478-0.418	2.9-4.9	V	CTIO	67;252;120	60	2.42	0.13 ± 0.05	6849.80986	18.6	566	Amor	6.80	...
2012 BF ₈₆	2016 Feb 22	91	1.043	0.0825	46.7-49.6	VR	DCT	71	15	0.0491	0.34 ± 0.04	7440.68168	22.6	89	Aten	10.14	...
2013 SB ₂₁	2013 Oct 14	64	1.031	0.034	12.4-12.5	wh	KP4	49	35	0.0584	0.83 ± 0.04	6579.77774	27.0	11	Amor	4.47	8.588
2013 SR	2013 Oct 14	51	1.050	0.070	40.5-40.6	wh	KP4	47	10	0.1305	1.00 ± 0.03	6579.63927	24.1	44	Amor	5.27	...
2013 TL	2013 Oct 14	89	1.022	0.085	70.7-70.8	wh	KP4	57	5	0.7942	0.56 ± 0.04	6579.97030	22.2	107	Apollo	5.89	...
2014 FF	2014 Mar 28	161	1.030	0.040	35.9-36.2	wh	KP4	72	8	0.1032	0.49 ± 0.03	6744.68831	24.2	42	Amor	6.51	...
2014 FR ₅₂	2014 Apr 18	85	1.135	0.148-0.147	20.1	wh	KP4	46	15	0.0149	0.37 ± 0.06	6765.66520	23.9	49	Amor	6.09	...
2014 HB ₁₇₇	2014 May 06	21	1.009	0.0034	87.1-87.8	VR	DCT	11	10	0.0239	1.05 ± 0.06	6783.97448	28.1	7	Apollo	4.83	6.752
2014 HE ₁₇₇	2014 May 06	69	1.056	0.049	17.0-16.9	VR	DCT	55	15	0.0897	0.25 ± 0.03	6783.65329	25.8	20	Amor	5.89	...
2014 HF ₅	2014 May 06	37	1.055	0.056	33.7-33.8	VR	DCT	45	20	0.1038	0.08 ± 0.03	6783.91201	25.3	25	Amor	5.92	...
2014 HN ₁₇₈	2014 Jun 16	144	1.032	0.044	67.7-67.9	r'	SOAR	142	10	0.0367	0.87 ± 0.02	6824.72654	23.5	59	Amor	5.58	...
2014 JD	2014 May 06	76	1.037	0.030	20.3-20.5	VR	DCT	52	7	0.0714	0.18 ± 0.04	6783.74905	26.3	16	Apollo	6.13	...
2014 JJ ₅₅	2014 Jun 03	52	1.073	0.086	45.2-45.3	VR	DCT	168	120	0.915	1.06 ± 0.03	6811.71253	25.3	25	Apollo	4.94	6.380
2014 JR ₂₅	2014 May 10–11	53	1.048-1.057	0.043-0.052	26.2-25.3	V	CTIO	106;75	45	0.487	0.26 ± 0.04	6787.73564	23.4	62	Apollo	7.65	...
2014 KA ₉₁	2014 Jun 04	64	1.034	0.026	40.9-41.0	wh	KP4	32	6	0.120	0.42 ± 0.04	6812.65859	25.5	23	Apollo	5.57	11.846
2014 KH ₃₉	2014 Jun 03	55	1.016	0.0051-0.0050	65.3-66.5	VR	DCT	50	1	0.0440	2.79 ± 0.02	6811.66803	26.2	17	Apollo	6.53	...
2014 OV ₃	2015 Feb 10	56	1.155	0.171	9.9-10.0	wh	KP4	121	70	0.3491	0.53 ± 0.02	7063.73463	23.2	68	Apollo	4.73	7.046
2014 TM ₃₄	2014 Oct 17	106	1.047	0.053-0.054	18.6-18.7	VR	DCT	57	15	0.0249	0.17 ± 0.03	6947.88390	25.0	29	Amor	5.58	...
2014 TP ₅₇	2014 Oct 17	71	1.024	0.028	15.6-15.5	VR	DCT	29	8	0.0137	0.16 ± 0.04	6947.64265	26.4	15	Amor	5.18	...
2014 UX ₇	2014 Oct 28	85	1.068	0.075	10.5-10.6	wh	KP4	102	45	0.0366	0.38 ± 0.04	6958.84348	25.6	22	Amor	5.26	7.294
2014 WU ₂₀₀ ^c	2014 Dec 01	60	0.996	0.011	16.1	wh	KP4	41	10	0.0179	0.27 ± 0.05	6992.72115	29.1	4	Apollo	4.17	4.206
2014 YT ₃₄	2015 Jan 13	124	1.012	0.037	38.9-39.5	r'	SOAR	133	5	0.1806	0.45 ± 0.02	7035.55787	24.7	34	Apollo	5.75	9.089
2015 CF	2015 Feb 11	157	1.069	0.086	15.7-15.8	VR	DCT	56	7	0.1841	0.05 ± 0.03	7064.87459	23.5	59	Amor	5.99	...
2015 HS ₁₁	2015 Apr 25	44	1.029	0.023	4.0-4.1	wh	KP4	44	7	0.0193	0.37 ± 0.04	7137.73600	27.1	11	Amor	4.29	6.683
2015 HU ₉	2015 May 08	128	1.099-1.098	0.130-0.129	43.8-44.2	wh	KP4	145	30	0.2130	0.15 ± 0.04	7150.66205	23.4	62	Apollo	8.24	...
2015 HV ₁₁	2015 May 08	55	1.072	0.068	22.1-22.0	wh	KP4	61	25	0.3102	0.20 ± 0.04	7150.89848	24.1	44	Amor	6.12	...
2015 JD	2015 May 08	98	1.022	0.016	36.1-35.7	wh	KP4	72	5	0.0339	0.07 ± 0.03	7150.79977	25.5	23	Apollo	6.00	11.965
2015 KE	2015 May 22	100	1.043	0.034	27.4-27.5	VR	DCT	66	5	0.0562	0.17 ± 0.03	7164.65626	26.4	15	Aten	4.54	4.296
2015 KM ₁₂₀	2015 May 26	166	1.042	0.050	54-53.9	wh	KP4	110	15	0.0296	0.19 ± 0.04	7168.66447	24.7	34	Amor	6.62	...
2015 KO ₁₂₂	2015 May 27	43	1.036-1.037	0.024	14.9-14.8	r'	SOAR	39	10	0.0648	0.17 ± 0.04	7169.83972	27.0	11	Apollo	6.78	...
2015 KQ ₁₂₀	2015 May 27	62	1.040	0.029	21.2-21.4	r'	SOAR	58	10	0.0898	0.98 ± 0.04	7169.87814	26.7	13	Apollo	4.89	10.883
2015 KW ₁₂₀	2015 May 26	159	1.037	0.024	10.5	wh	KP4	63	3	0.1355	0.24 ± 0.03	7168.76662	26.0	18	Apollo	6.20	...
2015 MX ₁₀₃	2015 Jun 29	129	1.045	0.039	42.2	r'	SOAR	111	8	0.7865	0.20 ± 0.04	7202.58034	24.4	39	Amor	5.36	...
2015 RF ₃₆	2015 Sep 14	146	1.053-1.052	0.057	34.5-34.3	wh	KP4	100	15	0.0123	0.14 ± 0.02	7279.93330	23.4	62	Aten	5.63	6.312
2015 RQ ₃₆	2015 Sep 14	69	1.058	0.058	25.6-25.5	wh	KP4	59	20	0.4812	0.23 ± 0.04	7279.87219	24.5	37	Apollo	5.13	...
2015 TL ₂₃₈	2015 Oct 24	52	1.035	0.042	16.4-16.5	VR	DCT	47	5	0.0713	0.46 ± 0.04	7319.68601	24.9	31	Apollo	7.43	...
2015 VE ₆₆	2015 Nov 24	126	1.005	0.021	32.7-33.3	r'	SOAR	101	2	0.037	0.38 ± 0.02	7350.71888	24.1	44	Amor	6.03	...

Table 1
 (Continued)

NEO	UT-Date	Nb_{im}	r_h (au)	Δ (au)	α ($^\circ$)	Filter	Tel	ΔT (minutes)	t_{exp} (s)	Rot. P. (hr)	Δm (mag)	φ_0 (2450000+)	H	D (m)	Dyn. class	ΔV_{SH} (km s $^{-1}$)	ΔV_{NHATS} (km s $^{-1}$)
2015 XF	2015 Dec 29	98	1.059	0.078	11.9-12.0	r'	SOAR	88	20	0.1003	0.51 ± 0.03	7385.75211	24.4	39	Amor	6.90	...
2016 AD ₁₆₆	2016 Jan 19	85	1.074	0.101	25.1-25.0	VR	DCT	49	15	0.0085	0.21 ± 0.03	7406.76968	23.6	56	Apollo	7.13	...
2016 AF ₁₆₆	2016 Jan 19	37	0.995	0.027	65.6-65.7	VR	DCT	14	10	0.0278	0.41 ± 0.05	7406.80902	25.4	24	Apollo	6.30	...
2016 AO ₁₃₁	2016 Jan 19	65	1.054	0.093	39.6	VR	DCT	27	10	0.0216	0.45 ± 0.04	7406.99723	24.1	44	Apollo	4.57	9.651
2016 AU ₉	2016 Jan 12	59	1.061	0.079	11.6	wh	KP4	135	30	0.594	0.59 ± 0.04	7399.87573	25.4	24	Amor	6.03	...
2016 AV ₁₆₄	2016 Jan 19	40	1.059	0.078	13.6	VR	DCT	15	10	0.0123	0.20 ± 0.04	7406.94935	24.9	31	Amor	6.24	...
2016 CS ₂₄₇	2016 Feb 22	108	1.019	0.033-0.034	27.2	VR	DCT	42	7	0.0514	0.12 ± 0.03	7440.85852	25.6	22	Apollo	4.43	8.076
2016 EL ₁₅₇	2016 Mar 16	50	1.013	0.018	8.7-8.9	VR	DCT	20	1	0.0198	0.19 ± 0.03	7463.89240	27.1	11	Apollo	6.36	...
2016 EN ₁₅₆	2016 Mar 16	94	1.009	0.014	8.7-8.6	VR	DCT	27	2	0.0863	0.44 ± 0.05	7463.91622	27.8	8	Apollo	4.98	9.108
2016 FL ₁₂	2016 Apr 07	46	1.032	0.032	17.3-17.4	r'	SOAR	47	9	0.3333	0.15 ± 0.05	7485.71234	26.3	16	Apollo	4.74	8.672
2016 FZ ₂	2016 Mar 22	139	1.1053	0.062	23.8-23.7	VR	DCT	49	5	0.0387	0.26 ± 0.05	7469.96281	24.5	37	Amor	6.62	...
2016 GW ₂₂₁	2016 Apr 19	113	1.041	0.043	30.3-30.0	r'	SOAR	98	3	0.2856	0.18 ± 0.05	7497.85083	24.8	32	Aten	7.43	9.526
2016 JP ₁₇	2016 May 09	95	1.029	0.032	52.3-52.0	VR	DCT	27	1	0.0702	0.65 ± 0.02	7517.78384	23.1	71	Apollo	6.17	...
2016 MA	2016 Jun 17	51	1.023	0.012	54.7-54.9	VR	DCT	29	5	0.0051	0.12 ± 0.04	7556.74356	27.5	9	Apollo	5.39	11.229
2016 NG ₃₈	2016 Jul 18	101	1.038	0.034	48-48.3	r'	SOAR	114	7	2.47	0.66 ± 0.04	7587.85278	25.1	28	Amor	5.98	...
2016 NK ₃₉	2016 Aug 15	74	1.070	0.085	45.9-46.1	r'	SOAR	107	30	1.46	0.24 ± 0.05	7616.49071	23.9	49	Amor	5.77	11.025
2016 PA ₄₀	2016 Aug 16	98	1.092	0.082	13.7-13.6	r'	SOAR	77	10	0.1375	0.93 ± 0.03	7616.86135	24.4	39	Apollo	7.16	11.513
2016 PP ₂₇	2016 Aug 16	116	1.080	0.081-0.082	32.7-32.8	r'	SOAR	95	5	1.55	0.26 ± 0.07	7616.69028	23.6	56	Apollo	7.12	...
2016 RB ₁	2016 Sep 07	198	1.009	0.0016-0.0012	30.9-28.5	VR	DCT	153	3	0.0267	0.21 ± 0.03	7638.82497	28.3	6	Aten	7.49	8.626
2017 EA ₃	2017 Mar 09	130	1.042	0.071	44.6-44.5	VR	DCT	65	5	0.71	0.05 ± 0.03	7821.75821	23.2	68	Apollo	6.72	...
2017 EE ₄	2017 Mar 15	106	1.000	0.019	71.6-72.1	VR	DCT	30	1	0.00699	0.31 ± 0.05	7827.99828	25.0	29	Apollo	6.00	...
2017 EH ₄	2017 Mar 09	139	1.056	0.070	25.3-25.2	VR	DCT	55	5	0.0624	0.56 ± 0.02	7821.69563	24.1	44	Amor	5.67	...
2017 FJ	2017 Mar 19	179	1.009-1.008	0.013	8.0	VR	DCT	49	5	0.0165	0.57 ± 0.03	7831.88047	28.2	6	Apollo	5.51	11.780
2017 FK	2017 Mar 19	108	1.005	0.085-0.084	17.7-18.1	VR	DCT	27	2	0.00428	0.30 ± 0.03	7831.72251	27.3	10	Apollo	5.61	9.042
2017 QG ₁₈	2017 Aug 27	296	1.032	0.024-0.023	22.0-21.8	VR	DCT	91	3	0.003298	0.21 ± 0.05	7992.64725	27.0	11	Apollo	5.26	11.411
2017 QK	2017 Aug 21	47	1.151	0.147	17.9	VR	SOAR	57	30	0.1599	0.20 ± 0.07	7986.54836	23.8	51	Apollo	5.45	...
2017 QT ₁	2017 Aug 21	158	1.030	0.020-0.019	19.5-20.1	VR	SOAR	70	10	0.77	0.78 ± 0.05	7986.69346	26.7	13	Apollo	8.07	...
<i>Complex</i>																	
2014 HS ₁₈₄	2014 Jun 02	89	1.069	0.061-0.060	24.0-24.1	V	CTIO	233	20	2.02	1.13 ± 0.04	6810.56578	23.3	65	Amor	5.72	...
2014 HW	2014 Apr 24	126	1.014	0.0089-0.0087	15.4	VR	DCT	108	4	0.0641	1.16 ± 0.03	6771.81914	28.4	6	Apollo	4.54	5.690
2016 BF ₁	2016 Jan 19	75	1.010	0.035	41.1-41.0	VR	DCT	54	10	0.2624	2.49 ± 0.02	7407.02439	25.4	24	Apollo	5.59	...
2016 DK	2016 Feb 22	285	1.048	0.108	54.5-54.6	VR	DCT	131	10	1.30	0.85 ± 0.02	7440.94528	22.4	98	Amor	11.34	...
2016 ES ₁	2016 Mar 16	99	1.089	0.095	9.9	VR	DCT	38	3	0.3484	0.26 ± 0.04	7463.94721	24.1	44	Amor	6.65	...
2017 EK	2017 Mar 15	35	0.995	0.017	86.5-86.6	VR	DCT	10	1	0.0064	1.59 ± 0.05	7827.99072	24.1	44	Apollo	7.03	...
2017 EZ ₂	2017 Mar 09	118	1.008	0.015	15.8-16.4	VR	DCT	39	3	0.0138	0.23 ± 0.03	7821.80369	25.1	28	Amor	8.75	...
2017 HV ₃	2017 Aug 27	278	1.081	0.102	44.1-43.9	VR	DCT	163	7	0.0881	0.77 ± 0.03	7992.87174	23.7	54	Amor	4.65	8.359
2017 JM ₂	2017 May 14	225	1.021	0.015	45.7-46.3	VR	DCT	67	2	0.0188	0.65 ± 0.02	7887.81127	24.3	41	Apollo	9.05	...
2017 KJ ₂₇	2017 May 28	76	1.023	0.019	60.4-61.0	VR	DCT	19	2	0.036	0.58 ± 0.03	7901.94000	25.4	24	Apollo	7.16	...
2017 LE	2017 Jun 04	224	1.031	0.019	33.1-32.7	VR	DCT	77	2	0.0281	0.39 ± 0.06	7908.85535	26.4	15	Amor	6.22	...
2017 MO ₈	2017 Jul 03	108	1.018-1.017	0.011	84.8-85.5	VR	DCT	34	1	0.0544	1.58 ± 0.03	7937.75364	26.0	18	Apollo	6.52	...
2017 QX ₁	2017 Aug 21	283	1.050	0.039	10.8-11.0	VR	SOAR	85	5	1.34	1.11 ± 0.02	7986.86290	24.8	32	Amor	5.53	...
<i>Partial light curve</i>																	
2013 VY ₁₃	2014 Jan 03	36	1.458	0.519	19.4	wh	KP4	118	180	>2	>0.1	6660.72197	21.2	171	Apollo	6.30	...
2013 XX ₈	2014 Feb 05	133	1.072	0.087	9.2-9.3	wh	KP4	128	30-45	>2.5	>0.6	6693.72231	24.4	39	Amor	4.57	10.364
2013 YS ₂	2014 Jan 27	122	1.023	0.057	45.9-45.8	wh	KP4	134	15	>2	>1.0	6684.60839	23.3	65	Amor	4.77	10.346

Table 1
(Continued)

NEO	UT-Date	Nb _{im}	r_h (au)	Δ (au)	α (°)	Filter	Tel	ΔT (minutes)	t_{exp} (s)	Rot. P. (hr)	Δm (mag)	φ_0 (2450000+)	H	D (m)	Dyn. class	$\Delta V_{\text{SH}}^{\text{SH}}$ (km s ⁻¹)	$\Delta V_{\text{NHATS}}^{\text{NHATS}}$ (km s ⁻¹)	
2014 FA ₇	2014 Mar 28	73	1.025-1.026	0.030	24.3	wh	KP4	127	60	>2	>0.2	6744.78622	26.7	13	Apollo	5.17	7.232	
2014 HK ₁₂₉	2014 May 08	164	1.198-1.199	0.261	39.1	wh	KP4	95	35	>3	>0.6	6785.63865	21.1	179	Apollo	6.26	...	
2014 WA ₃₆₆	2014 Dec 27	21	1.042	0.060	13.1	wh	KP4	19	45	>0.5	>0.5	7018.93337	26.9	12	Apollo	4.14	4.568	
2014 WO ₆₉	2014 Dec 01	66	1.131-1.131	0.149	11.2-11.3	wh	KP4	164	90	>2.5	>0.2	6992.83219	23.6	56	Amor	6.19	...	
2015 AA ₄₄	2015 Feb 10	116	1.010	0.052	61.8-62.1	wh	KP4	71	7	>1	>0.4	7063.66223	23.9	49	Apollo	5.68	...	
2015 ET	2015 Mar 14	132	1.018	0.026	20.0-19.9	wh	KP4	96	30	>2	>0.5	7095.88517	26.7	13	Apollo	6.48	...	
2015 GC ₁₄	2015 Apr 25	17	1.095	0.095	19.6	wh	KP4	39	40	>0.5	>0.3	7137.66520	24.8	32	Amor	5.29	...	
2015 PT ₂₂₇	2015 Aug 30	65	1.018-1.017	0.025	71.2-71.5	r'	SOAR	40	3	>1	>2.0	7264.88016	23.9	49	Apollo	6.29	...	
2015 QA	2015 Sep 03	85	1.112	0.110	19.0	VR	DCT	64	10	>1	>0.2	7268.68778	22.9	78	Amor	6.56	...	
2015 XA ₃₇₉	2016 Jan 12	9	1.026	0.049	27.1	wh	KP4	11	40	>0.2	>0.1	7399.77151	25.4	24	Amor	4.22	7.629	
2016 GF ₂₁₆	2016 May 17	19	1.058	0.051	24.7-24.6	VR	DCT	17	20	>0.5	>0.2	7525.85932	24.9	31	Amor	4.62	9.009	
2016 HN ₂	2016 May 09	95	1.103	0.114	33.3	VR	DCT	54	10-15	>1	>0.2	7517.92273	23.5	59	Apollo	6.08	...	
2016 HP ₃	2016 May 22	169	1.041	0.050	54.0-54.2	VR	DCT	60	5	>1	>1.0	7530.83529	23.7	54	Amor	6.46	...	
2016 JD ₁₈	2016 May 09	93	1.069	0.066	23.8	VR	DCT	36	10	>0.5	>1.3	7517.85625	24.7	34	Apollo	7.30	...	
2016 JE ₁₈	2016 May 09	176	1.036	0.027	9.4-9.3	VR	DCT	58	3-5	>1	>0.6	7517.80558	26.3	16	Amor	5.88	...	
2016 LO ₄₈	2016 Jun 15	72	1.041	0.032	36.5-36.6	VR	DCT	28	5-6	>0.5	>0.4	7554.78964	25.4	24	Amor	5.44	9.817	
2017 EK ₃	2017 Mar 09	216	1.025	0.033	14.1-13.8	VR	DCT	82	7-10	>1.5	>0.5	7821.85281	26.3	16	Apollo	5.87	8.840	
2017 QU ₁₇	2017 Aug 27	317	1.059	0.052	20.8-20.9	VR	DCT	105	5	>2	>0.2	7992.79683	26.1	17	Amor	6.20	...	
<i>Flat</i>																		
<i>light curve</i>																		
9	2008 HB ₃₈	2013 Oct 28	92	1.276-1.277	0.297-0.298	15.7	r'	KP2	136	40-60	6593.75162	21.1	179	Apollo	5.73	...
	2010 CF ₁₉	2013 Aug 16	11	1.127	0.128	25.2	V	CTIO	20	30	6520.71312	21.7	135	Apollo	5.46	9.449
	2012 ER ₁₄	2014 Feb 05	56	1.348	0.404-0.405	22.4	wh	KP4	145	90	6693.60084	20.5	236	Amor	5.43	...
	2013 PR ₄₃	2013 Sep 17	24	1.159-1.160	0.158	11.7-11.5	r'	SOAR	62	120	6552.76646	23.4	62	Apollo	5.11	...
	2013 SY ₁₉	2013 Oct 10	61	1.128	0.130	4.0	r'	SOAR	116	60	6575.76236	24.8	32	Amor	4.95	...
	2013 UE ₁	2013 Oct 30	97	1.033	0.049	35.0-35.2	r'	KP2	147	20-30	-	...	6595.72699	24.4	39	Apollo	5.96	...
	2013 UE ₃	2013 Oct 30	49	1.137	0.145	6.1-6.0	r'	KP2	97	50	6595.86569	22.7	85	Apollo	5.60	7.438
	2013 XY ₂₀	2014 Jan 03	118	1.011	0.045	52.1	wh	KP4	127	30	6660.97473	25.5	23	Amor	3.98	6.507
	2014 CS ₁₃	2014 Mar 25	30	1.235	0.257-0.258	20.1-20.2	VR	DCT	159	300	6741.77483	24.0	47	Apollo	5.36	8.754
	2014 KL ₂₂	2014 Jun 03	67	1.053	0.047	34.2	VR	DCT	41	10	6811.86838	24.6	35	Amor	5.76	11.740
	2014 OA ₂	2014 Aug 01	104	1.176	0.162	6.7-6.8	V	CTIO	145	30	6870.72426	21.3	163	Amor	5.86	...
	2014 QV ₂₉₅	2014 Sep 16	96	1.074	0.072	15.8	VR	DCT	76	10	6916.94185	24.9	31	Amor	6.32	...
	2014 TR ₅₇	2014 Oct 17	152	1.030	0.037	26.3-26.4	VR	DCT	95	6-15	6947.78720	25.2	27	Amor	5.48	...
	2014 UY ₇	2014 Oct 28	62	1.045	0.065	36.4	wh	KP4	98	35-40	6958.93640	24.8	32	Amor	6.44	...
	2014 WU _{200^b}	2014 Nov 26	68	1.003	0.016	9.1	VR	DCT	93	45-55	6987.79201	29.1	4	Apollo	4.17	4.206
	2014 WX ₂₀₂	2014 Nov 27	179	0.994	0.0075	13.4-13.3	VR	DCT	68	5	6988.95925	29.6	3	Apollo	4.09	4.151
	2015 KT ₅₆	2015 May 26	91	1.063	0.050-0.051	8.4-8.5	wh	KP4	73	15-20	7168.81786	26.1	17	Apollo	6.25	...
	2015 KV ₁₈	2015 May 26	108	1.135	0.127	14.3	wh	KP4	98	25	7168.87484	23.8	51	Amor	5.97	...
	2015 LK ₂₄	2015 Jun 29	201	1.040	0.060	65.0-65.3	r'	SOAR	147	5	7202.74810	21.6	142	Amor	7.82	...
	2015 RF ₂	2015 Sep 28	129	1.032	0.046	48.3-48.9	r'	SOAR	101	9	7293.55333	24.1	44	Apollo	6.59	...
	2016 AG ₁₆₆	2016 Jan 19	110	1.060	0.088	29.0-28.9	VR	DCT	40	5-10	-	...	7406.96436	24.0	47	Apollo	7.50	...
	2016 AU ₆₅	2016 Jan 19	117	1.146-1.145	0.164	8.0-8.2	VR	DCT	90	10	7406.70597	22.9	78	Aten	11.57	...
	2016 BE	2016 Jan 19	30	1.031	0.072	47.3	VR	DCT	22	25-40	7406.60448	23.7	54	Apollo	6.19	...
	2016 BJ ₁₅	2016 Feb 08	81	1.071	0.091-0.092	20.4-20.3	wh	KP4	156	20-30	7426.88096	23.3	65	Apollo	6.15	...
	2016 CF ₂₉	2016 Feb 08	92	1.032-1.031	0.051	26.5-27.0	wh	KP4	122	8-15	7426.79262	24.9	31	Apollo	7.22	...
	2016 CL ₂₉	2016 Feb 08	82	1.046	0.065	24.2-24.3	wh	KP4	80	15	7426.63062	24.6	35	Apollo	7.79	...

Table 1
(Continued)

NEO	UT-Date	Nb_{im}	r_h (au)	Δ (au)	α ($^\circ$)	Filter	Tel	ΔT (minutes)	t_{exp} (s)	Rot. P. (hr)	Δm (mag)	φ_0 (2450000+)	H	D (m)	Dyn. class	Δ_V^{SH} (km s^{-1})	Δ_V^{NHATS} (km s^{-1})
2016 EQ ₁	2016 Mar 16	50	1.028	0.033	5.7	VR	DCT	15	1–4	7463.93605	26.3	16	Apollo	4.73	9.915
2016 FX ₂	2016 Mar 22	71	1.033	0.058	49.2–49.1	VR	DCT	41	20	7469.64692	23.7	54	Apollo	4.52	8.014
2016 GB ₂₂₂	2016 Apr 19	145	1.017	0.016	37.4–38.1	VR	DCT	68	5	7497.81978	26.8	12	Apollo	5.84	...
2016 GV ₂₂₁	2016 Apr 19	201	1.013	0.026	69.6–70.3	VR	DCT	105	2–10	7497.63660	24.9	31	Apollo	5.49	10.590
<i>Tumblers</i>																	
2013 YG	2014 Jan 03	90	1.032	0.053	23.3–23.4	wh	KP4	97	15	0.2921	...	6660.82729	25.4	24	Aten	5.29	6.637
2014 DJ ₈₀	2014 Mar 26	120	1.043	0.059	38.3–38.6	r'	SOAR	166	45	6742.50997	26.3	16	Aten	4.41	5.527
2015 CG	2015 Feb 10	398	1.002	0.020	38.5–40.1	VR	DCT	134	3	0.0353	...	7063.91241	25.6	22	Apollo	6.58	...
2015 HB ₁₇₇	2015 May 12	114	1.023	0.035	67.3–67.7	VR	DCT	46	3	7154.93442	24.6	35	Apollo	6.61	11.795
2015 LJ	2015 Aug 18	136	1.066	0.061	26.8	VR	DCT	99	15–25	0.1875	...	7252.72284	24.7	34	Amor	4.36	8.404
2016 FA	2016 Mar 16	199	1.016	0.030	44.8–44.7	VR	DCT	57	3–5	7463.97424	25.2	27	Aten	5.96	6.918
2016 RD ₃₄	2016 Sep 15	190	1.008	0.0087	72.8–72.7	VR	DCT	79	2–5	0.0230	...	7646.84794	27.6	8	Amor	3.83	4.233
2017 EE ₃	2017 Mar 09	87	1.012	0.024	38.0–38.1	VR	DCT	30	5	0.1050	...	7821.73596	26.0	18	Apollo	5.64	...
2017 HU ₄₉	2017 May 14	274	1.022	0.014	36.5–37.0	VR	DCT	135	3–2	0.62	...	7887.65057	26.5	14	Aten	4.49	4.473
2017 QW ₁	2017 Aug 21	121	1.047	0.036	15.4–15.5	VR	SOAR	68	15	0.0987	...	7986.74562	26.2	17	Aten	4.82	5.171

Notes.

^a UT-date, distance Sun-object (r_h), and distance Earth object (Δ), and phase angle (α) are summarized. The filter (details in Thirouin et al. 2016), telescope (Tel) and number of images (Nb_{im}), rotational period (Rot. P. in hour), relative amplitude (Δm), and the Julian Date (φ_0) for the zero phase are presented. No light-time correction is applied. Absolute magnitude (H), and an estimate of the NEO diameter (D) with 20% as albedo are also reported. Exposure time (t_{exp}), and duration of the observing block (ΔT) for each NEO are indicated.

^b Two other light curves have been published for this object by Warner (2015c), suggesting a rotational period of 31 hr and by Kikwaya Eluo (2018) with a periodicity of 1 hr. For the purposes of our work, we use the MANOS result reported here.

^c Two light curves are reported for this object (Section 4).

(This table is available in machine-readable form.)

Benner et al. 2015). Assuming that small NEOs are following the same tendency as NEOs with $D > 200$ m, some MANOS NEOs are potentially oblate. Oblate objects appear to have long rotational periods that are consistent with/longer than the length of our runs. Therefore, some of our flat light curves are potentially caused by oblate objects. Unfortunately, as there is no estimate for the quantity of oblate rotators (independent of size) or if small NEOs have the tendency to be oblate, we cannot propose a clear percentage.

4.4. Fast Rotators

The periodicities of small NEOs ($D < 100$ m) may be undetected as a result of “long” exposure times. For example, we report two light curves for 2014 WU₂₀₀. One of the light curves is flat, but the second displays periodic photometric variations. The first light curve was obtained on 2014 November 26th at DCT. The visual magnitude of 2014 WU₂₀₀ was 20.7 mag (MPC estimate). Due to the faintness and bad atmospheric conditions, we selected an exposing time of 45–55 s (+read-out of 13 s). The typical photometry error bar was 0.03 mag for the DCT data. With the Mayall Telescope we reobserved this object few days later when the magnitude was 20.1 mag (MPC estimate). In this case, we employed 10 s as the exposure time (+11 s of read-out time), and we favored a rotation of ~ 64 s. The typical photometry error bar was 0.05 mag for the Mayall data. Therefore, the exposing time used at DCT was too long to derive such a short period.

Some of our objects with flat light curves were imaged with exposing times between 30 and 300 s. These values were selected for a decent signal-to-noise ratio, but these times may not have been optimal to sample the light curve and so no periodic photometric variations were detected. We estimate that 23 MANOS NEOs are maybe fast to ultra-rapid rotators whose rotations were undetected due to a “long” exposing time and/or the bad weather conditions.¹³ Small NEOs are commonly rotating fast (Figure 2), and if so, 52% of our flat light curves from this work and Thirouin et al. (2016) are potentially due to small ultra-rapid/fast rotators.

For fast/ultra-rapid NEOs rotating over a few seconds or few minutes, the exposure time is important. Following Pravec et al. (2000), the optimum exposure time ($T_{\text{exp}}^{\text{opt}}$) to detect a light curve with two harmonics is

$$T_{\text{exp}}^{\text{opt}} = 0.185 \times P, \quad (2)$$

with P as the object’s periodicity (Section 2 of Pravec et al. 2000). This relation is based on theory and does not reflect a specific observing strategy. Because we know the exposing time during our observations, we can figure out the detectable rotational period. For example, with $T_{\text{exp}} = 11$ s, we will perfectly sample the light curve of a small body rotating in 1 minute or more. In this case, an object rotating in $\ll 1$ minute will have a flat light curve and thus its rotation will be undetectable.

In Figure 3, the continuous line is for Equation (2) for a perfectly sampled two harmonic light curve. The data points are MANOS NEOs imaged with our 4 m facilities. Objects below the continuous line have oversampled light curves, whereas above this line the light curves are undersampled. The

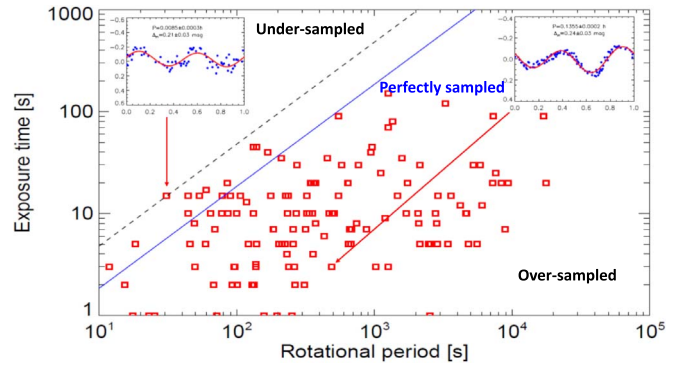


Figure 3. The red squares are the MANOS objects with a rotational period estimate. The blue continuous line indicates the relation between exposure time and rotational period for a perfectly sampled light curve with two harmonics. Objects below this line have an oversampled light curve, and objects above it have an undersampled light curve. Some MANOS objects have an under-sampled light curve, but we were able to derive their rotational period. See Section 4 for more details.

dashed line in Figure 3 represents an empirical upper limit to the period-exposure time relationship using the MANOS data set and can be articulated as

$$T_{\text{exp}}^{\text{MANOS}} = 0.48 \times P. \quad (3)$$

This relation would converge to Nyquist sampling theory in a regime of infinite signal-to-noise ratio. For the smallest objects, and thus potentially fast to ultra-rapid rotators, using Equation (3) we can identify the rotational period to which we were sensitive based on object-specific exposure time. Using Equations (2) and (3), we have two lower limits for the potential rotational periods. Therefore, if these objects have a rotational period between these two estimates, we should have detected it. In conclusion, the rotational period is likely shorter than the estimate and thus we undetected it in our observing block (assuming that the objects have a two-harmonics light curve). But it is also important to emphasize that some small objects (sub-100 m objects), even if they are expected to rotate fast, might be slow rotators (Figure 2).

5. Physical Constraints

A strengthless rubble-pile will not be able to rotate faster than about 2.2 hr without breaking up (Pravec et al. 2002). But most small NEOs have rotational periods of a few seconds or minutes. Therefore, an explanation for these rapid rotations is that NEOs are bound with tensile strength and/or cohesion instead of just gravity. Using Holsapple (2004, 2007), we calculated the maximum spin limits assuming different densities and tensile strength coefficients for the NEO population. Following Richardson et al. (2005), we considered a friction angle of 40° , and moderately elongated ellipsoids ($c/a = b/a = 0.7$). We used two values for the density; 2 (Itokawa (Fujiwara et al. 2006)) and 5 g cm^{-3} (density of a stony-iron object (Carry 2012)), and two tensile strength coefficients, 10^5 , and $10^6 \text{ N m}^{-3/2}$ (with a range of tensile strengths for Almahata Sitta; Kwiatkowski et al. 2010). Five MANOS targets require a tensile strength coefficient between 10^5 – $10^6 \text{ N m}^{-3/2}$: 2014 FR₅₂, 2014 PR₆₂, 2015 RF₃₆, 2016 AD₁₆₆, and 2016 AO₁₃₁.

¹³ Only objects observed with our 4 m class facilities are considered, as most of our data are from 4 m class telescopes.

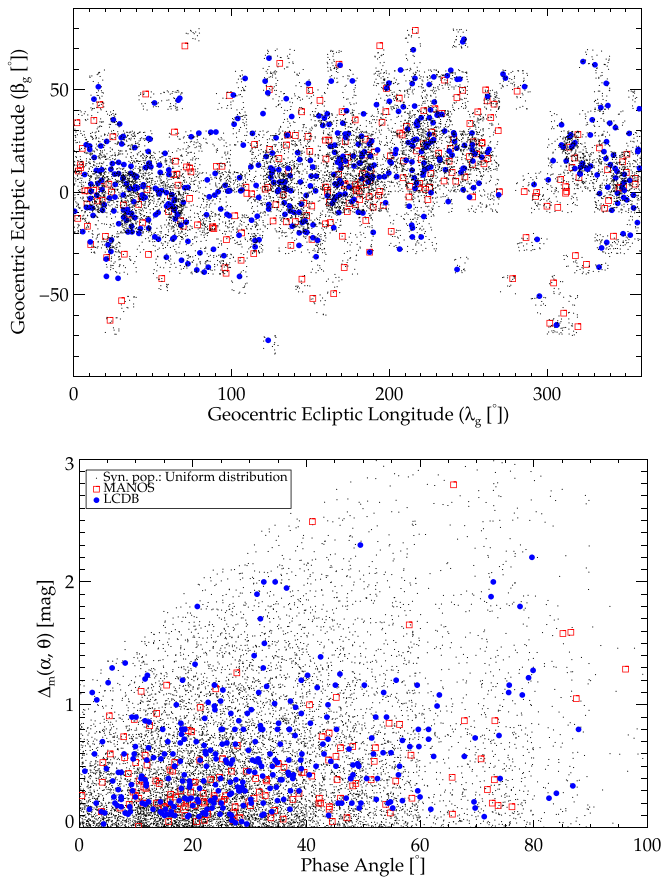


Figure 4. We used the MANOS+LCDB sample (red squares+blue circles) to create a distribution of geocentric ecliptic coordinates for our synthetic population (black dots). As the aspect angle is unknown for our objects, we express the light-curve amplitude as a function of phase angle. Following the procedure presented in Section 7, the lower panel reports the light-curve amplitude biased by the phase angle of our synthetic population in the case of a uniform distribution of axis ratio. We overplotted the MANOS and LCDB samples for comparison. The synthetic population and the observations are in agreement.

The light-curve amplitudes ($\Delta m(\alpha)$) in Table 1 were obtained at a phase angle α . At $\alpha = 0^\circ$, the amplitude is

$$\Delta m(\alpha = 0^\circ) = \frac{\Delta m(\alpha)}{1 + s\alpha}, \quad (4)$$

with $s = 0.03 \text{ mag deg}^{-1}$ (Zappala et al. 1990). In the MANOS sample, only 12 objects (10% of our sample) have a $\Delta m(\alpha = 0^\circ) \geq 0.5 \text{ mag}$, and one object has a $\Delta m(\alpha = 0^\circ) \geq 1 \text{ mag}$. In the LCDB, there are 309 NEOs¹⁴ with an absolute magnitude $H \geq 20 \text{ mag}$, that are observed at a phase angle $\alpha \leq 100^\circ$: 47 of them have a $\Delta m(\alpha = 0^\circ) \geq 0.5 \text{ mag}$ (15% of the LCDB), and 6 have a $\Delta m(\alpha = 0^\circ) \geq 1 \text{ mag}$ (2%). Therefore, the relative abundance of high amplitude light curves in these two data sets is consistent.

¹⁴ The observing circumstances or light curve amplitude are not reported for some LCDB objects, and thus they are not considered here. Only NEOs with a $H \geq 20 \text{ mag}$ are considered because MANOS focuses on small objects. We select objects observed at a phase angle lower than 100° because MANOS is observing in that range.

6. Potential Mission Targets

One of our goals is to find favorable target(s) for a future mission to a NEO, and thus mission accessibility is one of our selection criteria (Abell et al. 2009; Hestroffer et al. 2017; Bambach et al. 2018). For this purpose, we estimate the velocity change for a Hohmann transfer orbit also known as Δv . A rough guess of the Δv is estimated with the Shoemaker & Helin (1978) protocol (Δv^{SH}). In order to obtain an accurate estimate, one can use the Near-Earth Object Human Space Flight Accessible Targets Study (NHATS) orbital integration, Δv^{NHATS} .¹⁵ NHATS uses specific constraints to compute the Δv^{NHATS} (i) launch before 2040, (ii) total mission duration ≤ 450 days, and (iii) number of days spent at the object ≥ 8 days. The NHATS limit is Δv^{NHATS} of 12 km s^{-1} . Several of our targets do not follow these criteria, so no Δv^{NHATS} are available for them (Table 1).

According to NHATS, 78 MANOS NEOs are accessible with a spacecraft (Table 2, and Table 2 in Thirouin et al. 2016). For diverse reasons, Abell et al. (2009) found that the best target for a mission should have a moderate to slow rotation ($P > 1 \text{ hr}$). Only 9 MANOS NEOs have such a long rotation, have a $\Delta v^{\text{NHATS}} \leq 12 \text{ km s}^{-1}$; and have been observed for spectroscopy (Table 2, and Table 2 in Thirouin et al. 2016). We will present spectral results for these objects in future publication(s).

Finally, we note that several non-fully characterized MANOS NEOs have a new optical window in the upcoming years or decades. For example, the low Δv^{NHATS} and slow rotator 2013 XX₈ (spectral type unknown) will have a new optical window in 04/2019, thus we will have an opportunity to fully characterize this potential target.

7. MANOS+LCDB Versus Synthetic Population

In this section, we aim to compare our results to a synthetic population of NEOs to identify biases regarding our measured amplitude distribution and to constrain the distribution of morphologies in the NEO population. In a first step, we create 10,000 synthetic objects and calculate their light-curve amplitude versus aspect angle. In a second step, we “observationally sample” this synthetic population based on prescribed phase angles, in order to compare our synthetic population with the MANOS+LCDB data set.

Step 1: Assuming that NEOs are prolate ellipsoids (with $b = c$) at a phase angle of 0° , the amplitude varies as

$$\Delta m(\theta) = 1.25 \times \log \left[\frac{1}{\cos^2 \theta + (b/a)^2 \sin^2 \theta} \right], \quad (5)$$

where θ is the aspect angle, and b/a is the elongation of the object (Michalowski & Velichko 1990). The aspect angle is

$$\cos \theta = -\sin \beta_g \sin \beta_p - \cos \beta_g \cos \beta_p \cos(\lambda_g - \lambda_p), \quad (6)$$

where β_p and λ_p are the object’s north pole ecliptic latitude and longitude, and λ_g and β_g are the object geocentric ecliptic coordinates (Michalowski & Velichko 1990). We use Equation (5) to generate the light-curve amplitude of 10,000 synthetic objects. The only two free parameters in this equation are the axis ratio b/a and the viewing angle θ . In theory, the axis ratio b/a varies from 0 to 1. However, for objects visited

¹⁵ <http://neo.jpl.nasa.gov/nhats/>

Table 2
Most Suitable Targets for a Robotic/Human Mission^a

NEO	H	Diameter [m]	Rot. Period [hr]	Vis. Spec.	Δ_v^{SH}	Δ_v^{NHATS}	Start Next Optical Window
2016 DK	22.4	98	1.30	no	11.34
2017 QX ₁	24.8	32	1.34	yes	5.53
2016 NK ₃₉	23.9	49	1.46	no	5.77	11.025	2023/05
2016 PP ₂₇	23.6	56	1.55	yes	7.12
2014 HS ₁₈₄	23.3	65	2.02	yes	5.72
2010 MR	18.6	566	2.42	no	6.80
2016 NG ₃₈	25.1	28	2.47	no	5.98
2015 AA ₄₄	23.9	49	>1	no	5.68
2015 QA	22.9	78	>1	no	6.56
2015 PT ₂₂₇	23.9	49	>1	yes	6.29
2016 HN ₂	23.5	59	>1	yes	6.08
2016 HP ₃	23.7	54	>1	no	6.46
2016 JE ₁₈	26.3	16	>1	no	5.88
2017 EK ₃	26.3	16	>1.5	no	5.87	8.840	none
2015 ET	26.7	13	>2	no	6.48
2013 VY ₁₃	21.2	171	>2	yes	6.80
2013 YS₂	23.3	65	>2	yes	4.77	10.346	2020/09
2014 FA₇	26.7	13	>2	yes	5.17	7.232	2032/09
2017 QU ₁₇	26.1	17	>2	no	6.20
2013 XX ₈	24.4	39	>2.5	no	4.57	10.364	2019/04
2014 WO ₆₉	23.6	56	>2.5	yes	6.19
2014 HK ₁₂₉	21.1	179	>3	yes	6.26

Note.

^a MANOS obtained spectra and light curves for two good spacecraft targets (italic/bold), but we also summarize all NEOs with a rotational period longer than 1 hr. For completeness purposes, Δ_v^{SH} and Δ_v^{NHATS} following the Shoemaker & Helin (1978) protocol and the NHATS parameters are summarized. The start of the next opportunity to observe these objects according to NHATS is also shown (<https://cneos.jpl.nasa.gov/nhats/>).

by spacecraft, Eros¹⁶ is the most elongated with a ratio $b/a = 0.32$ (Veverka et al. 2000). Thus, we limit the axis ratio b/a between 0.32 and 1 (spherical object). We considered three possible axis distributions for our synthetic population: (i) a uniform distribution of b/a , (ii) one distribution with an excess of spheroidal objects, and (iii) one with an excess of elongated objects (Figure 5, upper panel).

The second parameter is the aspect angle θ ranging from from 0° to 90° (absolute value). La Spina et al. (2004) and Vokrouhlický et al. (2015) noticed an excess of retrograde-rotating NEOs (based on a limited sample), which would imply that the observed distribution of pole orientations is not uniform. We updated the distribution of poles reported in Vokrouhlický et al. (2015) with the newest results from the LCDB (multiple systems have been excluded from the distribution, as we do not expect any small NEO as binary/multiple, Margot et al. 2002). With the newest results, the pole distribution is still consistent with the Vokrouhlický et al. (2015) result. Using our updated pole distribution, we created a non-uniform distribution of pole orientation and thus a distribution of $(\lambda_p; \beta_p)$. Even though most of the objects with a known pole orientation are large objects, and we assume that the pole orientation of the small objects is similar to that of large objects, this assumption might be wrong and will need to be tested once more pole orientations of small objects are known. The typical uncertainty on pole orientation is about $\pm 10^\circ$ based on radar and light-curve inversion results, so we estimated the number of objects within a grid of

$10^\circ \times 10^\circ$. We use the number density of objects in this grid of pole coordinates to randomly assign a pole orientation to each of our 10,000 synthetic objects.

Equation (6) also depends on the geocentric ecliptic coordinates $(\lambda_g; \beta_g)$. For the MANOS sample, we use the zero phase of our light curve to estimate the $(\lambda_g; \beta_g)$ of our objects. In order to present the most accurate sample, we also incorporated the LCDB objects with $H > 20$ mag. Unfortunately, authors generally did not report the zero phase timing of their light curves, so we used approximate coordinates for those objects based on the observing nights reported in the literature. Once $(\lambda_g; \beta_g)$ were estimated for the MANOS+LCDB sample, we created a grid of geocentric ecliptic coordinates of $10^\circ \times 10^\circ$. Such a grid allowed us to take into account the approximate coordinates of the LCDB objects.¹⁷ Therefore, we created a distribution of $(\lambda_g; \beta_g)$ based on the observations from the MANOS+LCDB sample (Figure 4, upper plot). Using this and the distribution of $(\lambda_p; \beta_p)$, we calculated the distribution of aspect angles (Equation (6)), which were then used as input to Equation (5) to calculate a synthetic population of light-curve amplitudes at zero phase.

Step 2. As the aspect angles of our observed sample are unknown, we cannot directly compare our data set and the synthetic population. However, we can effectively observe our synthetic objects by assigning a phase angle based on the observed distribution of phase angles for MANOS+LCDB objects. By merging Equations (4) and (5), we estimate the light-curve amplitude of our synthetic population at these

¹⁶ Only objects visited by spacecraft were taken into account because of the direct estimate of their size/axis ratio.

¹⁷ For observations during close approach, some objects may move more than $10^\circ \times 10^\circ$ and thus are not in the right grid; however, this applies to a small number of objects and will not change the main conclusions of our simulations.

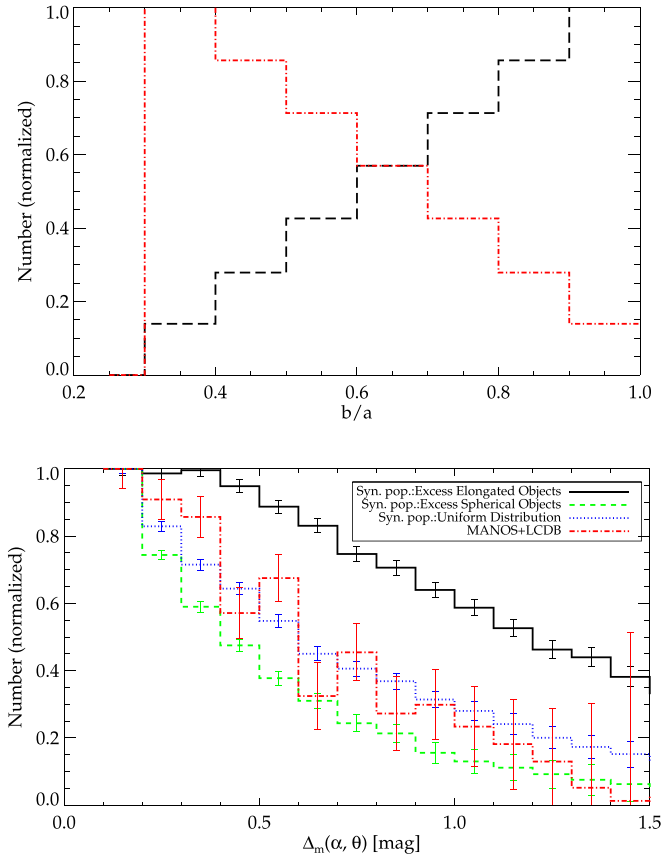


Figure 5. We consider two non-uniform distributions of b/a (upper panel) with an excess of elongated objects or an excess of spheroidal objects. Following the procedure presented in Section 7 the other plots report the light-curve amplitude non-corrected from phase angle of the two synthetic distributions, as well as the MANOS+LCDB sample. The lower panel focuses on objects with an amplitude between 0.1 and 1.5 mag. The error bars are $\sqrt{1/N}$, with N being the number of objects per bin.

prescribed phase angles. In Figure 4, we plot the MANOS sample and the LCDB objects with a $H > 20$ mag and a phase angle lower than 100° . We limit this analysis to small objects observed at a phase angle between 0° and 100° in order to mimic the MANOS sample. Based on Figure 4 (lower plot), it is obvious that the MANOS and LCDB observations are not uniform with phase angle. In fact, both data sets have an excess of objects observed at low/moderate phase angle (up to $\sim 40^\circ$), and only a handful of objects are observed at high phase angle ($\alpha > 80^\circ$). Drawing from the distribution of MANOS+LCDB objects, we create a non-uniform distribution of phase angles for our synthetic population (Figure 4, lower panel), and then calculate the amplitude of our 10,000 synthetic objects.

In Figure 5 (lower panel), we plot the normalized histogram of light-curve amplitude for the synthetic population and the MANOS+LCDB samples. The error bars are $\sqrt{1/N}$, with N being the number of objects per bin. We limit our distribution to light-curve amplitudes up to 1.5 mag, as only a handful of objects with higher light-curve amplitudes are reported. Generally, objects with low light-curve amplitude are difficult to obtain, as they require a large amount of observing time under good weather conditions. In addition, observers have the tendency to not report or publish flat light curves. Therefore,

there is a clear bias in the LCDB regarding these low-amplitude objects, thus we do not take into account objects with a light-curve amplitude < 0.1 mag.

In Figure 5 (lower panel), we plot our three synthetic populations (uniform distribution of b/a , an excess of spherical objects and an excess of elongated objects) for amplitudes between 0.1 and 1.5 mag. In order to compare the simulated population and the observed sample, we calculate the χ^2 per degree of freedom:

$$\frac{\chi^2}{\nu} = \frac{1}{\nu} \sum_i^n \left[\frac{f(\Delta m_i) - \Delta m_i}{\sigma_i} \right]^2, \quad (7)$$

where ν is the degree of freedom, Δm_i are the observed data, $f(\Delta m_i)$ are the simulated results, and σ_i are the uncertainties (i is the index of the bin and n is the bin number). Comparing the MANOS+LCDB data with the excess of elongated object distribution, we find a χ^2/ν of 2.67. The MANOS+LCDB sample compared to the excess of spherical object distribution gives us a χ^2/ν of 1.17, whereas compared to the uniform distribution the χ^2/ν is 0.31. This suggests that a uniform distribution of b/a best fits the observed sample. Our model assumes a basic uniform distribution of b/a for prolate ellipsoids. Future improvements to this model could employ more realistic shapes based on radar observations and/or light-curve inversion.

8. Summary/Conclusions

We report full light curves for 57% of our sample (82 NEOs), and constraints for the amplitude and period are reported for 21 NEOs. Thirty NEOs do not exhibit any periodic variability in their light curves. We also report 10 potential tumblers.

MANOS found a potential new ultra-rapid rotator: 2016 MA. This object has a potential periodicity of 18.4 s. The confidence level of this periodicity is low and more data are required to confirm this result. Unfortunately, there is no optical window to re-observe this object until 2025, and even then it only reaches $V \sim 22.5$ mag. We also uncovered the fastest rotator to date, 2017 QG₁₈ rotating in 11.9 s.

Several MANOS targets display a flat light curve. Because of the well-known relation between size and rotational period, we can infer that large objects ($D > 100$ m) are slow rotators and their rotational periods were undetected during the amount of observing time dedicated. Based on this size-dependent cut, we estimate that 43% of our flat light curves are slow rotators with a rotational period longer than our observing blocks. A flat light curve of a small NEO can be attributed to fast/ultra-rapid rotation which goes undetected because of the long exposing time used to retrieve a good signal-to-noise ratio. We suggest that 52% of our flat light curves are potential fast/ultra-rapid rotators. We use the size of the object as a main criteria for these findings. This is an acceptable approximation, but may not be true for all the objects.

We present a simple model to constrain the light-curve amplitude distribution within the NEO population. One of the main parameters of our model is the b/a axis ratio of an object. We create several axis distributions, using a uniform distribution as well as an excess of spherical and elongated objects. Assuming that the pole orientation distribution reported in

Vokrouhlický et al. (2015) is representative of the NEO population, we generate 10,000 synthetic ellipsoids. We inferred that an uniform distribution of b/a best matches the observed sample. This suggests that the number of spherical NEOs is roughly equivalent to the number of highly elongated objects.

A total of 78 MANOS objects are mission accessible according to NHATS, which assumes a launch before 2040. However, considering only fully characterized objects, and NEOs rotating in more than 1 hr, our sample of viable mission targets is reduced to nine objects: 2002 DU₃, 2010 AF₃₀, 2013 NJ, 2013 YS₂, 2014 FA₇, 2014 FA₄₄, 2014 YD, 2015 FG₃₆, and 2015 OV. Two of these nine objects will be bright enough during their next observing windows for new and complementary observations: 2013 YS₃ will have a $V \sim 18$ mag in 2020 December–January, and the visual magnitude of 2002 DU₃ will be 20.6 mag in 2018 November.

The authors acknowledge the referee for useful comments that improved this work. Lowell operates the Discovery Channel Telescope (DCT) in partnership with Boston University, the University of Maryland, the University of Toledo, Northern Arizona University, and Yale University. Partial support of the DCT was provided by Discovery Communications. LM was built by Lowell Observatory using funds from the National Science Foundation (AST-1005313). This work is also based on observations obtained at the Southern Astrophysical Research (SOAR) telescope, which is a joint project of the Ministério da Ciência, Tecnologia, e Inovação (MCTI) da República Federativa do Brasil, the U.S. National Optical Astronomy Observatory (NOAO), the University of North Carolina at Chapel Hill (UNC), and Michigan State University (MSU). We also used the 1.3 m SMARTS telescope operated by the SMARTS Consortium. This work is based in part on observations at Kitt Peak National Observatory, National Optical Astronomy Observatory (NOAO Prop. ID:2013B-0270), which is operated by the Association of Universities for Research in Astronomy (AURA) under cooperative agreement with the

National Science Foundation. This research has made use of data and/or services provided by the International Astronomical Union’s Minor Planet Center. The authors acknowledge support from NASA NEOO grants NNX14AN82G, and NNX17AH06G. D. Polishook is grateful to the Ministry of Science, Technology and Space of the Israeli government for their Ramon fellowship for post-docs.

Appendix A

Examples of Lomb periodograms for an object reported in this work.

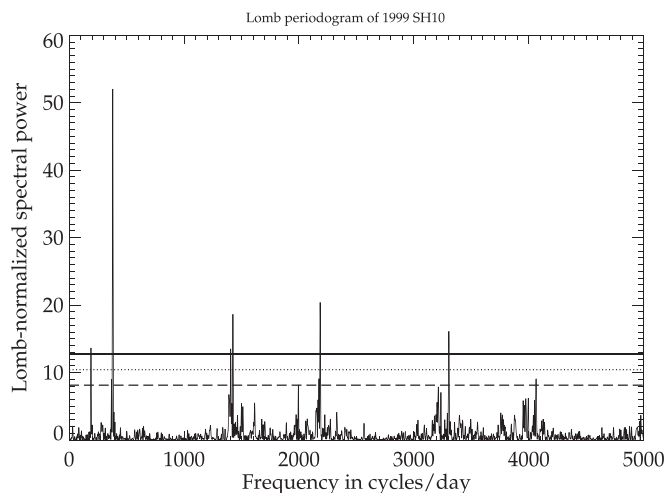


Figure 6. Example Lomb periodogram of 1999 SH10. Lomb periodograms are plotted with several confidence levels (continuous line: 99.9%; dotted line: 99%; and dashed line: 90%).

(The complete figure set (86 images) is available.)

Appendix B

Examples of the light curves of objects reported in this work.

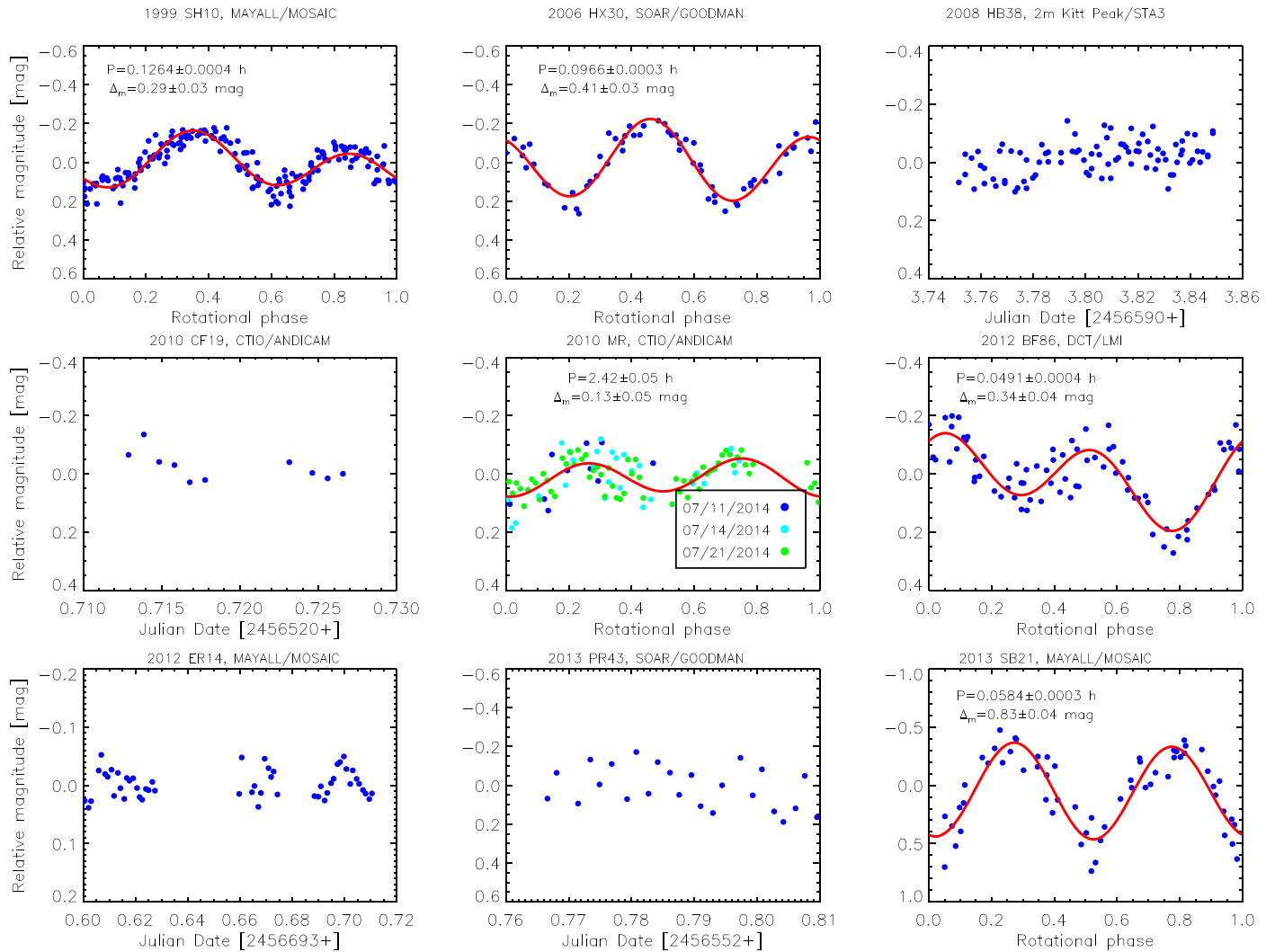


Figure 7. Example MANOS light curve results are plotted. Light curves and photometry files can be found at manos.lowell.edu.

(The complete figure set (16 images) is available.)

ORCID iDs

Audrey Thirouin  <https://orcid.org/0000-0002-1506-4248>

Nicholas A. Moskovitz  <https://orcid.org/0000-0001-6765-6336>

David Trilling  <https://orcid.org/0000-0003-4580-3790>

References

- Abell, P. A., Korsmeyer, D. J., Landis, R. R., et al. 2009, *M&PS*, **44**, 1825
- Bambach, P., Deller, J., Vilenius, E., et al. 2018, arXiv:1805.01750
- Benner, L. A. M., Busch, M. W., Giorgini, J. D., Taylor, P. A., & Margot, J.-L. 2015, in *Asteroids IV*, ed. P. Michel, F. E. DeMeo, & W. F. Bottke (Tucson, AZ: Univ. of Arizona Press), 165
- Brozović, M., Benner, L. A. M., Taylor, P. A., et al. 2011, *Icar*, **216**, 241
- Busch, M. W., Ostro, S. J., Benner, L. A. M., et al. 2011, *Icar*, **212**, 649
- Carry, B. 2012, *P&SS*, **73**, 98
- Fujiwara, A., Kawaguchi, J., Yeomans, D. K., et al. 2006, *Sci*, **312**, 1330
- Hanuš, J., Ďurech, J., Brož, M., et al. 2013, *A&A*, **551**, A67
- Hestroffer, D., Agnan, M., Segret, B., et al. 2017, *AGUFM*, P11F-05
- Holsapple, K. A. 2004, *Icar*, **172**, 272
- Holsapple, K. A. 2007, *Icar*, **187**, 500
- Kikwaya Eluo, J.-B. 2018, *ASSP*, **51**, 27
- Kwiatkowski, T., Polinska, M., Loaring, N., et al. 2010, *A&A*, **511**, A49
- Lacerda, P., & Luu, J. 2003, *Icar*, **161**, 174
- La Spina, A., Paolicchi, P., Kryszczyńska, A., & Pravec, P. 2004, *Natur*, **428**, 400
- Li, J.-Y., Helfenstein, P., Buratti, B., Takir, D., & Clark, B. E. 2015, in *Asteroids IV*, ed. P. Michel, F. E. DeMeo, & W. F. Bottke (Tucson, AZ: Univ. of Arizona Press), 129
- Margot, J. L., Nolan, M. C., Benner, L. A. M., et al. 2002, *Sci*, **296**, 1445
- Michalowski, T., & Velichko, F. P. 1990, *AcA*, **40**, 321
- Nolan, M. C., Magri, C., Howell, E. S., et al. 2013, *Icar*, **226**, 629
- Ostro, S. J., Margot, J.-L., Benner, L. A. M., et al. 2006, *Sci*, **314**, 1276
- Pravec, P., & Harris, A. W. 2007, *Icar*, **190**, 250
- Pravec, P., Harris, A. W., & Michalowski, T. 2002, in *Asteroids III*, ed. W. F. Bottke Jr. et al. (Tucson, AZ: Univ. of Arizona Press), 113
- Pravec, P., Harris, A. W., Scheirich, P., et al. 2005, *Icar*, **173**, 108
- Pravec, P., Hergenrother, C., Whiteley, R., et al. 2000, *Icar*, **147**, 477

- Pravec, P., Scheirich, P., Kušnirák, P., et al. 2006, *Icar*, **181**, 63
- Reddy, V., Dunn, T. L., Thomas, C. A., Moskovitz, N. A., & Burbine, T. H. 2015, in *Asteroids IV*, ed. P. Michel, F. E. DeMeo, & W. F. Bottke (Tucson, AZ: Univ. of Arizona Press), 43
- Richardson, D. C., Elankumaran, P., & Sanderson, R. E. 2005, *Icar*, **173**, 349
- Shoemaker, E. M., & Helin, E. F. 1978, in *Reports of Planetary Geology Program*, 20
- Taylor, P. A. 2009, PhD thesis, Cornell Univ.
- Thirouin, A., Moskovitz, N., Binzel, R. P., et al. 2016, *AJ*, **152**, 163
- Veverka, J., Robinson, M., Thomas, P., et al. 2000, *Sci*, **289**, 2088
- Vokrouhlický, D., Bottke, W. F., Chesley, S. R., Scheeres, D. J., & Statler, T. S. 2015, in *Asteroids IV*, ed. P. Michel, F. E. DeMeo, & W. F. Bottke (Tucson, AZ: Univ. of Arizona Press), 509
- Warner, B. D. 2014, *MPBu*, **41**, 157
- Warner, B. D. 2015a, *MPBu*, **42**, 256
- Warner, B. D. 2015b, *MPBu*, **42**, 41
- Warner, B. D. 2015c, *MPBu*, **42**, 115
- Warner, B. D., Harris, A. W., & Pravec, P. 2009, *Icar*, **202**, 134
- Zappala, V., Cellino, A., Barucci, A. M., Fulchignoni, M., & Lupishko, D. F. 1990, *A&A*, **231**, 548